POLITECNICO DI TORINO
Repository ISTITUZIONALE

Hidden soils and their carbon stocks at high-elevation in the European Alps (North-West Italy)

Original
Hidden soils and their carbon stocks at high-elevation in the European Alps (North-West Italy) / Pintaldi, E.; D'Amico, M. E.; Colombo, N.; Colombero, C.; Sambuelli, L.; De Regibus, C.; Franco, D.; Perotti, L.; Paro, L.; Freppaz, M.. - In: CATENA. - ISSN 0341-8162. - ELETTRONICO. - 198:(2021). [10.1016/j.catena.2020.105044]

Availability:
This version is available at: 11583/2854427 since: 2020-12-02T14:28:27Z

Publisher:
Elsevier B.V.

Published
DOI:10.1016/j.catena.2020.105044

Terms of use:

This article is made available under terms and conditions as specified in the corresponding bibliographic description in the repository

Publisher copyright

(Article begins on next page)

21 September 2024

*Manuscript
Click here to view linked References

Hidden soils and carbon stocks in high-elevation ecosystems in the Alps (NW-Italy)

Emanuele Pintaldi[1,*], Michele E. D'Amico[1], Nicola Colombo[1,2,3], Chiara Colombero[4], Luigi Sambuelli[4], Claudio De Regibus[4], Diego Franco[4], Luigi Perotti[3], Michele Freppaz[1,2]

[1]University of Turin, Department of Agricultural, Forest and Food Sciences (DISAFA), Largo Braccini, 2, 10095 Grugliasco (TO), Italy.

[2]University of Turin, Research Center on Natural Risk in Mountain and Hilly Environments (NatRisk), Largo Braccini, 2, 10095 Grugliasco (TO), Italy.

[3]University of Turin, Department of Earth Sciences (DST), Via Valperga Caluso, 35, 10125 Turin, Italy.

[4]Politecnico di Torino, Department of Environment, Land and Infrastructure Engineering (DIATI), Corso Duca degli Abruzzi, 24, 10129 Turin, Italy.

Abstract

Alpine soils, especially those covered by vegetation and/or with permafrost, store large quantities of total organic carbon (TOC). Given their high vulnerability to climate change, they may release large amounts of CO_2 in a warming scenario. Thus, it is important to know their C stock in order to understand its possible release. While C stocks of forest and alpine grassland soils are well documented, little is known about soils and C stocks in high-elevated periglacial environments dominated by cryoturbation. The object of this study is the periglacial environment of the Stolenberg Plateau (LTER site Istituto Mosso, 3030 m a.s.l.), at the foot of the Monte Rosa Massif (NW Italian Alps). The plateau is covered by a thick stony layer, organized in periglacial blockfields and blockstreams. The plant cover reaches only 3-5%. During the construction of a chair lift, the opening of trenches revealed, unexpectedly, extremely well-developed soils under the active periglacial stone cover. In particular, thick (30-65 cm) and dark TOC-rich A horizons were observed. Below these umbric horizons, cambic Bw ones were developed but discontinuous. Despite the lack of vegetation, C stocks were surprisingly high (up to ~5 kg*m^{-2}), comparable to vegetated soils at lower elevation. Non-invasive geophysical methods revealed that these hidden soils were widespread on the plateau under the stony cover, with a mean thickness around 50 cm. These TOC-rich soils, without vegetation and covered by periglacial landforms, represent a unique pedoenvironment suggesting new perspectives on the actual C-stocks in high-elevation ecosystems, which are probably underestimated.

Keywords

Soil organic matter; Periglacial; Blockstream/Blockfield; Geophysics

1 Introduction

Soil Organic Matter (SOM) stored in alpine soils is a fundamental part of the global C cycle (Prietzel and Christophel, 2014), acting as a sink for carbon dioxide and having therefore a great potential to sequestrate this from the atmosphere (Bojko and Kabala, 2017). Alpine soils, especially those covered by vegetation and/or with permafrost, store large quantities of organic carbon (e.g., Celi et al., 2010; Bockheim and Munroe, 2014). However, given the high vulnerability of soils to climate change (Schröter et al., 2005; Hagedorn et al., 2010), they may release large amounts of carbon dioxide in a warming scenario (e.g., Schuur et al., 2013; Knowles et al., 2019).

High-elevation soils are dominated by cryoturbation processes, induced by seasonal frost penetration or permafrost, leading to the formation of patterned ground, typical of periglacial environments (e.g., tilting of stones, blockstreams, blockfield, wedges, etc.). As it is mostly driven by temperature, active patterned ground is vulnerable to climate warming, which can induce several possible effects such as permafrost degradation (e.g., Biskaborn et al., 2019; Mollaret et al., 2019), expansion of plant cover and transition from pioneer species towards more acidophilous grassland (e.g., Gerdol and Smiraglia, 1990; D'Amico et al., 2015), and increased SOM decomposition (e.g., Álvarez Arteaga et al., 2008; Cheng et al., 2012).

While the carbon stocks of forest and alpine grassland soils are well documented by several studies (e.g., Leifeld et al., 2009; Zollinger et al., 2013; Bockheim and Munroe, 2014), very little is known about carbon stocks in high-elevated periglacial environments, especially in the European Alps. This is probably due to different reasons, such as: 1) these soils are located in very unfavourable conditions at high elevation and they are often difficult to reach, requiring specific technical equipment; 2) generally, these high-elevation surfaces are not covered by vegetation therefore, considering plants as first carbon source, these soils received less interest since they are not considered a relevant carbon sink compared to forest soils; 3) high-elevation soils are typical of periglacial environments, which are characterized by cryoturbation processes (induced by low temperatures and/or permafrost) that allow the formation of patterned ground. Thus, they are frequently covered by coarse debris which makes it difficult to recognize them as soils and perform in-depth pedological investigations using manual devices.

In order to deepen the investigation on these high-elevation pedoenvironments, geophysical methods can be used thanks to their capability to map soil thickness and distribution even in areas of intricate relationships between soil and top or bottom enclosing geological materials, undulating topography, and non-homogeneous or anisotropic material properties. Among the available geophysical methods, Electrical Resistivity Tomography (ERT) allows investigating contrasts in electrical properties between the soil material (loose, porous, prone to water retention and possibly rich in organic matter) and massive bedrock or coarse glacial deposits. The same contrast in physical and mechanical properties, together with differences in layering and internal structure, can be imaged using Ground Penetrating Radar (GPR) profiling. ERT and GPR are widely used to support pedological surveys for soil classification, mapping of the presence, depth and lateral variability of soil horizons, agricultural purposes and contamination analyses from low to mid latitudes and elevations (e.g., Samouelian et al., 2005; Allred et al., 2008; Doolittle and Butnor, 2009; Andre et al., 2012; Nováková et al., 2013). By contrast, few applications of geophysical prospections for the study of high-elevation soils are reported in the literature. In periglacial environments, these techniques are mainly used for permafrost characterization, hydrogeological processes and soil-bedrock interface recognition (Moorman et al., 2003; Otto and Sass, 2006; Kneisel et al. 2008; McClymont et al., 2010; Léger et al., 2017).

The study area is located in the severe periglacial environment of the Stolenberg Plateau (3030 m a.s.l., LTER site Istituto Mosso) on the southern slope of Monte Rosa Massif (4634 m a.s.l., NW Italian Alps) where, in 2017, the operational activities for a new chair lift construction inside a blockfield/blockstream area revealed unexpected well-developed soils. Considering the impossibility to deepen the investigation using manual devices and machinery, and the necessity to detect the distribution of these hidden soils, non-invasive geophysical methods were applied in September 2019.

Based on previous considerations, this work aims at: 1) describing and classifying the buried soils, 2) evaluating their carbon stock, and 3) investigating their distribution and thickness.

2 Materials and Methods

2.1 Study Area

The work was carried out in the periglacial environment of the Stolenberg Plateau, located at 3030 m a.s.l., at the boundary between Valle d'Aosta and Piemonte regions (Fig. 1), at the foot of the southern slope of Monte Rosa (4634 m) (NW Italian Alps). The research area represents the summit portion of the Long Term Ecological Research (LTER) site Angelo Mosso Scientific Institute (LTER-Italia IT19-001-T), belonging to the LTER-Italy network. The study area is also a Site of Community Importance and a Special Protection Area (SCI/SPA IT1204220 "Ambienti glaciali del gruppo del Monte Rosa") (Directive, 1992) belonging to the Natura 2000 network.

From 2007 to 2018, the area had a mean annual air temperature of –2.3 °C, a mean cumulative annual snowfall of 818 cm, and a mean annual liquid precipitation of ca. 400 mm. Snow cover lasts for at least 8 months, reaching a maximum thickness of ca. 350 cm (Freppaz et al., 2019).

During the snow-free season, the area shows typical features of periglacial environments, characterized by active periglacial landforms. In particular, the plateau is covered by a thick layer of stones with variable size (from decimetric to metric), well organized in blockfields, blockstreams/sorted stripes, gelifluction lobes, tilted stones and weakly developed sorted circles (Fig. 1). The activity of the morphology is evidenced by the absence of lichens from most stones (Ballantyne and Matthews, 1982). The parent material is composed of gneiss and mica-schists (Monte Rosa nappe, Pennidic basement) and metabasites (Zermatt-Saas unit).

The vegetation cover, which is almost absent or confined to small patches reaching no more than 5% of the plateau areal extension, is composed mainly of alpine species such as *Silene acaulis, Carex curvula, Salix herbacea* in the vegetated patches, while *Festuca halleri, Poa alpina, Ranunculus glacialis, Leuchantemopsis alpina, Cerastium uniflorum* and a few other pioneer species grow also in the stone-covered area, with extremely low cover values.

2.2 Soil survey sampling and analysis

In 2017, during the operational activities for a new chair lift construction, the largest part of the plateau was delimited in order to protect the natural environment (Directive, 1992) and the periglacial features from the excavation operations. However, three trenches were opened (2-10 m long, to a depth of around 1.2 m) in the construction area, revealing unexpected, well-developed soils under the stony cover. This finding was possible only thanks to the machinery employed, which utilization was exceptionally allowed for the construction of the chair lift station.

Field description of soils transect was performed according to FAO (2006), while soil classification was done according to WRB classification system (FAO, 2014). Three soil profiles were described and sampled, named P1, P2 and P3 (Fig. 1). Overall, 27 soil samples were collected from the profiles. The samples were air-dried, sieved to 2 mm and analyzed following the standard methods reported by Van Reeuwijk (2002). The pH was measured in water (soil: water = 1:2.5). The particle-size analysis was performed by the pipette method after organic matter destruction with H_2O_2 followed by dispersion with Na-hexametaphosphate. Total carbon (corresponding to total organic carbon-TOC due to the absence of carbonates) and nitrogen (TN) concentrations, were measured by dry combustion with an elemental analyzer (CE Instruments NA2100, Rodano, Italy).

The soil organic carbon stock (C-STOCK$_{tot}$ kg*m^{-2}) of the profiles was calculated for sectors in which the horizons sequence was similar, according to the following equation adapted from Batjes (1996):

$$C - STOCKtot = \sum_{i=1}^{n} \frac{\mathrm{TOC*BD*TH*VF}}{1000} \tag{1}$$

where n is the number of soil horizons of each sector, TOC is the soil organic carbon concentration (g*kg^{-1}) of the mineral horizons, BD is the Bulk Density (kg*m^{-3}) based on mean Bulk Density values of high-elevation soils (D'Amico et al., submitted) measured according to Boone et al. (1999), TH is the horizon thickness (m), VF is the volume of fine earth excluding the coarse mineral fraction (> 2 mm), calculated as [1 − (% rock volume/100)], 1000 is the unit correction factor.

In order to support the interpretation of the geophysical measurements, the clay mineralogy was analysed using a Philips PW1710 X-ray diffractometer (40kV and 20 mA, CoKα radiation, graphite monochromator). The Mg saturated clay fraction (< 2 μm) was separated by sedimentation, flocculated with $MgCl_2$, washed until free of Cl^-, and freeze-dried. Scans were made from 3 to 35 °2θ at a speed of 1 °2θ min^{-1}, on air dried, ethylene glycol solvated, and heated (350° and 550 °C) oriented mounts. A semi-quantitative evaluation of mineral abundance was performed using the Mineral Intensity Factors method (Islam and Lotse, 1986), which considers peak areas. For the calculation, the background was subtracted and the peak positions, intensities and areas were calculated using the PowderX software (Dong, 1999).

2.3 Geophysical investigation

Six 48-electrode Electrical Resistivity Tomography (ERT) profiles were acquired (Fig. 1). Five of them had an inter-electrode spacing of 0.30 m, for a total length of 14.1 m. One longer profile (ERT 3 in Fig. 1) was acquired with a spacing of 2 m between the electrodes, for a total length of 94 m. Short profiles were aimed at the detection and lateral imaging at shallow depths of the buried soils with high-resolution, while the longer line was designed for a deeper general low-resolution characterization of the bedrock conditions on which the soil horizons lay. Electrodes were georeferenced using a Garmin GPS 60 system to retrieve the position of each survey line on a high-resolution digital surface model (DSM) of the plateau and later account for topographic variations in the inversion of the longest ERT line, for which differences in height between the electrodes were significant. Digital vertical and slantwise photos obtained from an Unmanned Aerial Vehicle (UAV) survey were processed with structure from motion and multi-view-stereo algorithms to produce a high-resolution DSM (10 cm / pixel ground resolution) of the investigated area (cf., Smith et al. 2015; Carrivick et al., 2016, Alberto et al., 2018) (Supplementary Material, SM1).

ERT data were acquired with a multichannel resistivity meter (Syscal Pro - Iris Instruments). The acquisition scheme included 870 Wenner-Schlumberger array configurations along each line. On each quadrupole, measurements were repeated between 5 and 10 times, to reach a standard deviation of the average measured values lower than 5%. Raw data were manually filtered basing on their related standard deviation and inverted with Res2DInv software (Loke and Barker, 1996). On the resulting electrical resistivity sections, total gradient computations were implemented to detect marked depth and lateral variations and highlight the distribution and continuity of the soil material. To constrain data interpretation, tests on the electrical resistivity of the soil material were carried out on site in an uncovered soil outcrop (approximately 1.5 x 0.3 m) with a single quadrupole with 0.25-0.30- and 0.40-m electrode spacing and eight array configurations of current and potential electrode positions. The results were statistically analysed to retrieved average reference values of the electrical resistivity of the target material.

Ten ground penetrating radar (GPR) profiles (Fig. 1) were complementary acquired with a 500-MHz antenna controlled by an IDS K2 digital acquisition unit. GPR traces were acquired for a total time of 100 ns and 512 samples per trace respectively. Ublox EVK-5T GPS was used to track each survey position. The average distance between subsequent traces resulted in 0.025 m along each line. A standard data processing sequence was carried out in Reflexw software (Sandmeier), involving: i) dewow, to reduce very low frequency components; ii) band-pass Butterworth filtering around the central frequency of each antenna; iii) move start time, to remove the delay introduced by the system; iv) time cut at 50 ns, to reduce the trace length after a check on the deterioration of the S/N ratio with time (depth); v) manual gain to recover trace amplitude with time (depth); vi) background removal to reduce the effect of horizontal banding in the radargrams.

Local rare diffraction hyperbola in the radargrams were fitted with a velocity of 0.1 m/ns. To apply this value for time-to-depth conversion, the medium velocity (v) was additionally estimated by the Complex Refractive Index Method (CRIM, Birchak et al., 1974; Wharton et al., 1980), following:

$$\sqrt{\varepsilon_S} = (1-\varphi)\sqrt{\varepsilon_m} + \varphi\, S \sqrt{\varepsilon_w} + \varphi\,(1-S)\sqrt{\varepsilon_a} \qquad (2)$$

and

$$v = \frac{c}{\sqrt{\varepsilon_S}} \qquad (3)$$

where ε_S, ε_m, ε_w and ε_a are the relative dielectric permittivities of soil, soil matrix, pore water and air respectively, φ is the soil porosity, S is the degree of water saturation and $c=3 \cdot 10^8$ m/s (electromagnetic wave velocity in vacuum). In Equation 2, $\varepsilon_a=1$, $\varepsilon_w=77.8$ (from GPR measurements on the water of a nearby pond; Colombo et al., 2018) and $\varepsilon_m=7$ (from average reference values of similar loamy sandy soils, e.g., Daniels, 2004). Soil porosity φ was indirectly estimated from density measurements in the range 0.5 to 0.6. Moist (unsaturated) conditions were present on site during GPR acquisitions. A variable S, between 0.2 and 0.4, was consequently considered in the computation. Using these parameters, average $\varepsilon_S=9.3$ and v=0.10 m/ns were obtained for time-to-depth conversion. The approximate wavelength of a 500-MHz GPR signal in this material is consequently 0.2 m, meaning approximately 0.1 m of vertical resolution (half wavelength) in the investigated medium.

3 Results and interpretation

3.1. Soil profiles characteristics

Below a 10-60 cm thick stony/blocky layer (blockfields and blockstreams, respectively on flat surfaces or on gentle slopes), the profiles were characterized by thick (between 30 and 65 cm) and continuous dark A horizons with subangular-blocky, platy or granular structure (Table 1, Fig. 2, 3 and 4). These horizons were characterized by few roots and an extremely weak biogenic structure, where present, and they were classified as umbric horizons according to WRB. Below the umbric horizons, cambic Bw ones were often developed although discontinuous, characterized by brown colour and well-expressed subangular-blocky structure (Table 1, Fig. 2, 3 and 4). Cryoturbation features, such as inclusions of surface A materials at depth and convolutions and block displacement above wedges, were often observed within the profiles; thick, dense silt caps were also observed on the upper faces of stone fragments. The soil profiles were classified as Skeletic Umbrisol (Arenic, Turbic), according to FAO (2014).

3.2 Soils physical and chemical properties

The soil texture was generally loamy sandy or sandy loamy, with a substantial prevalence of sand (77% on average) compared to silt (20%) and clay (3%) fractions (Tab. 1). The clay fraction was composed of ca. 60% quartz, 20% mica/illite, 10% chlorite, 10% plagioclase and other minerals in traces (not shown). pH values were extremely to moderately acidic, ranging between 4.3 and 5.9. TOC content spanned from 0 to over 20 g*kg^{-1}, reaching maximum values in A horizons, while TN values were very low in all the samples. The TOC/TN ratio ranged between 7 and 20, reaching maximum values in the A horizons.

Considering the overall C-STOCK$_{tot}$ of each sector within the profiles (Table 2, Fig. 2, 3 and 4), in P1 the values ranged between 0.7 and over 5 kg*m^{-2}, reaching minimum and maximum values in sector C and A respectively; in the profile P2 the values spanned from 1.12 to approx. 3 kg*m^{-2} reaching minimum values in sector D and maximum in sector F; the C-STOCK$_{tot}$ of P3 reached the minimum value of 2.17 kg*m^{-2} in sector K and a maximum of 3.30 in kg*m^{-2} in the sector I.

3.3 Geophysical investigation

Results obtained from the long ERT line (ERT3 in Fig. 5a) provided a non-homogeneous electrical resistivity distribution in the plateau bedrock. The deepest values (5-7 kΩ m in the line centre below 5-m depth, yellow in Fig. 5a) were interpreted as representative of compact bedrock. Higher resistivities (>7 kΩ m, green in Fig. 5a) were depicted at shallower depths, reaching values of 15 kΩ m in proximity of the fractured overhanging rock cliff delimiting the plateau eastern edge. These values were related to variable fracturing conditions of the shallow bedrock, increasing towards E and NE. Relatively low electrical resistivity values, also considering the lithology of the area and its fracturing conditions, pointed towards the absence of relevant bodies of permafrost in the investigated area (cf., Kneisel, 2006).

Above the fractured bedrock, all the short ERT lines revealed the presence of a distinct and discontinuous layer with variable thickness under the stony cover, with resistivity values lower than 5 kΩ m (red in Fig. 5, b to d). Separated measurements acquired on an uncovered soil outcrop showed resistivity values in the range 2.9-4.2 kΩ m for the soils of interest, with an average of 3.6 kΩ m over 24 tests with different array spacing and electrode configuration. Consequently, this shallow layer was interpreted as representative of the soil presence under the periglacial cover.

The GPR profiles depicted a complex stratigraphy in the first meters of depth. Exemplificative results are reported in Fig. 6 for the GPR profiles acquired along the ERT lines of Fig. 5. Processed radargrams were visually interpreted as shown in Fig. 6a. In the shallower part of each section, GPR reflections appear as laterally continuous, smooth and sub-horizontal, likely due to the soil presence (s in Fig. 6a). Below this layer, intricate patterns of discontinuous GPR reflections are conversely present, more steeply dipping in different directions. This layer (t in Fig. 6a) possibly corresponds to the transition between soil and bedrock. The chaotic arrangement of soil material and debris resulting from the fractured bedrock may have generated this complex GPR response. At depths higher than 1 m, GPR reflections show again a more homogeneous lateral continuity, possibly indicating the bedrock presence (b in Fig. 6a).

Given the difficulty and subjectivity in manually picking the soil bottom from GPR sections (Fig. 6, b, d and f), ERT results (Fig. 5) were transformed in total gradient sections of electrical resistivities. The gradient maxima in each section were then automatically picked and interpreted as objective markers of the presence of a sharp vertical and lateral contrast between soil and surrounding materials and consequently used to estimate the average soil thickness in the plateau. Results are shown in Fig. 6 (c, e and g) in comparison with manual picking performed on GPR sections. Electrical resistivity gradient maxima generally fall within the transition layer (Fig. 6a) depicted in GPR results, providing a rough estimate of the soil bottom interface. The soil presence was detected by both geophysical methods within the first meter of depth of all the investigated lines.

4 Discussion

4.1 Soil properties and carbon stocks

The opening of trenches revealed the unexpected presence of complex and well-developed soils (Umbrisols) under the stony cover, with convolutions and inclusions of different materials, as a result of intense cryoturbation processes (Bockheim and Tarnocai, 1998). Despite the strong geomorphic activity characterizing this periglacial area, the observed soils were extremely well developed, particularly inside periglacial landforms (blockfields and blockstreams). Considering the remarkable thickness of A horizons (up to 60 cm), these soils resulted also more developed then the surrounding and vegetated soils at similar or lower elevation, where weakly developed and shallow

Skeletic Regosols, Cambisols or Umbrisols (e.g., Magnani et al., 2017) with thinner A horizon (up to 25-30 cm) were common. The textural class as well as the pH values were comparable to those found in the surrounding soils under snowbed vegetation (e.g., Magnani et al., 2017).

Considering the absence of a significant vegetation cover on the plateau, the high elevation and the presence of the thick stony cover, the estimated total carbon stock for each sector was surprisingly high. Overall, the results were comparable to carbon stock values reported for high-elevation, cryoturbated soils in the Aosta Valley, although generally covered by alpine tundra, for which values around 2-3 kg*m^{-2} (D'Amico et al., submitted) were reported. The values were also in the range reported for other vegetated soils in Alpine tundra ecosystems (Bockheim and Munroe, 2014). However, our results, in particular from P1, despite the lack of vegetation, were also in the normal range of carbon stock values from moderately developed forest or heath soils in the Aosta Valley, such as Entic Podzols (D'Amico et al., submitted), and to those reported by Chiti et al. (2012) for forest ecosystems in Spain, or for mountain boreal forests in North America (Hoffmann et al., 2014). In addition, on Italian Alps, very few works reported similar soils with C-rich A horizons at high elevation (around 3000 m a.s.l.) (e.g., Baroni et al., 1996).

4.2 Soil distribution, depth and subsurface morphology of the plateau

Geophysical investigations confirmed the widespread presence of soils on the whole plateau. Considering the soil texture, the measured electrical resistivity values (2-5 kΩ m) may appear unusually high for field tests carried out in moist (but unsaturated) conditions on these materials. Since the presence of minerals having relevant surface conductivity was found to be almost negligible (i.e. illite and chlorite are less than 1% of the total solid matrix), a rough check on the expected soil electrical resistivity ρ_S can be performed following Archie's law (Archie, 1942):

$$\rho_S = a \frac{\rho_w}{\varphi^m S^k} \qquad (4),$$

where ρ_w is pore water resistivity (around 100 Ω m, i.e. moisture mainly due to precipitation and shallow seepage), a=1 and m=1.4 are Archie's coefficients for non-consolidated sediments (Archie, 1942; Friedman, 2005), φ is the soil porosity (0.5 to 0.6), S is the degree of water saturation and k coefficient can be assumed equal to 2 for S>0.1. Applying Equation 4, retrieved ρ_S values are in the range 1.3-6.5 kΩ m for S between 0.2 and 0.4, thus additionally confirming the obtained electrical resistivity values.

Thanks to the electrical resistivity gradient maxima analyses, the soil bottom was recognized at depths ranging from 26 to 88 cm, for an average of 47 cm over the five short ERT lines. In general, higher depths (and soil thicknesses) were identified in the eastern part of the plateau (ERT2 in Fig. 1), close to the chair lift station, in presence of a more fractured underlying bedrock and below a particularly coarse stone cover. By contrast, the lowest depths were found in the grassy area on the northern side of the plateau, where periglacial blockfields/blockstreams are absent (ERT6 in Fig. 1). A decrease in soil thickness was also observed close to the rock outcrops present in the plateau. Even if ERT surveys had lower vertical resolution with respect to GPR profiles, soil depth and thickness estimations from electrical resistivity gradient maxima were straightforward and provided a less subjective estimation in these complex subsurface settings.

Considering the remarkable thickness of soil layer and its wide distribution, it is possible to assume that the overall C-stock of the plateau may be higher than estimated. In particular, the southern and south-western portions of the plateau are covered by a particularly coarse and thick block cover, which resembles the eastern part where the soil thickness and C stocks are larger. In addition, although not expressed in the results, a negative relation between soil organic carbon content and resistivity was detected.

5 Conclusion and perspectives

During the operational activities for a new chair lift construction at the Stolenberg Plateau, the opening of soil trenches revealed, unexpectedly, the presence of extremely well-developed soils under a thick stony cover consisting of periglacial blockfields and blockstreams. These soils, classified as Umbrisol, were characterized by surprisingly high C stocks, comparable to alpine tundra or even forest soils, despite the lack of vegetation and the presence of the stony cover. The application of non-invasive geophysical methods revealed that these hidden soils were widespread on the plateau under the stony cover, with a mean thickness around 50 cm, that generally increase where the periglacial features were more expressed (up to ca. 90 cm).

These C-rich soils, without vegetation and covered by periglacial landforms, may represent a unique pedoenvironment suggesting new perspective on the actual C stocks in high-elevation ecosystems, which are probably underestimated. In addition, the origin of these C-rich soils below blockstreams and blockfields, apparently in contrast with present day condition, may be of great relevance for unravelling the history of the high-elevation landscape of the Monte Rosa alpine area. For instance, they could be buried paleosols below moving stone layers, retaining therefore information about past climate. An alternative explanation could also be related to reduced decomposition of organic matter associated with the cooling effect caused by the stone cover. A more precise characterization of the organic matter, its age and species has indeed to be performed by further studies in the area.

Acknowledgements

This study was supported by European Regional Development Fund in Interreg Alpine Space project Links4Soils (ASP399): Caring for Soil—Where Our Roots Grow. (http://www.alpinespace.eu/projects/links4soils/en/the-project). Many thanks to Monterosa Ski Resort (project stakeholder) for providing logistical support.

References

Alberto, W., Palomba, M., Perotti, L., 2018. SMART GROUND project test-sites topographic and morphologic characterization: Instruments and methodologies. Rendiconti Online Società Geologica Italiana 46, 107–114.

Allred B.J., Daniels J.J., Ehsani M.R., 2008. Handbook of Agricultural Geophysics. CRC Press Taylor Francis Group, Boca Raton.

Andre F., van Leeuwen C., Saussez S., van Durmen R., Bogaert P., Moghadas D., de Resseguier L., Delvaux B., Vereecken H.; Lambot S., 2012. High-resolution imaging of a vineyard in south of France using ground penetrating radar, electromagnetic induction and electrical resistivity tomography. Journal of Applied Geophysics, 78: 113–122.

Archie, G.E., 1942. The electrical resistivity log as an aid in determining some reservoir characteristics. Trans. Am. Inst. Mech. Eng. 146, 54–67.

Arteaga, G.Á., Calderón, N.G., Krasilnikov, P.V., Sedov, S.N., Targulian, V.O., Rosas, N.V., 2008. Soil altitudinal sequence on base-poor parent material in a montane cloud forest in Sierra Juárez, Southern Mexico. Geoderma 144, 593–612.

Ballantyne, C.K., Matthews, J.A., 1982. The development of sorted circles on recently deglaciated terrain, Jotunheimen, Norway. Arctic and Alpine Research 14, 341–354.

Baroni, C., Orombelli, G., 1996. The Alpine “Iceman” and Holocene Climatic Change. Quat. res. 46, 78–83. https://doi.org/10.1006/qres.1996.0046

Batjes, N.H., 1996. Total carbon and nitrogen in the soils of the world. Eur J Soil Science 47, 151–163. https://doi.org/10.1111/j.1365-2389.1996.tb01386.x

Birchak, J.R., Gardner, C.G., Hipp, J.E., and Victor, J.M., 1974. High dielectric constant microwave probes for sensing soil moisture: Proc. IEEE, 62, 93-98.

Biskaborn, B.K., Smith, S.L., Noetzli, J., Matthes, H., Vieira, G., Streletskiy, D.A., Schoeneich, P., Romanovsky, V.E., Lewkowicz, A.G., Abramov, A., Allard, M., Boike, J., Cable, W.L., Christiansen, H.H., Delaloye, R., Diekmann, B., Drozdov, D., Etzelmüller, B., Grosse, G., Guglielmin, M., Ingeman-Nielsen, T., Isaksen, K., Ishikawa, M., Johansson, M., Johannsson, H., Joo, A., Kaverin, D., Kholodov, A., Konstantinov, P., Kröger, T., Lambiel, C., Lanckman, J.-P., Luo, D., Malkova, G., Meiklejohn, I., Moskalenko, N., Oliva, M., Phillips, M., Ramos, M., Sannel, A.B.K., Sergeev, D., Seybold, C., Skryabin, P., Vasiliev, A., Wu, Q., Yoshikawa, K., Zheleznyak, M., Lantuit, H., 2019. Permafrost is warming at a global scale. Nat Commun 10, 264. https://doi.org/10.1038/s41467-018-08240-4

Bockheim, J.G., Munroe, J.S., 2014. Organic Carbon Pools and Genesis of Alpine Soils with Permafrost: A Review. Arctic, Antarctic, and Alpine Research 46, 987–1006. https://doi.org/10.1657/1938-4246-46.4.987

Bockheim, J.G., Tarnocai, C., 1998. Recognition of cryoturbation for classifying permafrost-affected soils. Geoderma 81, 281–293.

Bojko, O., Kabala, C., 2017. Organic carbon pools in mountain soils — Sources of variability and predicted changes in relation to climate and land use changes. CATENA 149, 209–220. https://doi.org/10.1016/j.catena.2016.09.022

Boone R.D., Grigal D.F., Sollins P., Ahrens R.J., Armstring, D.E., 1999. Soil sampling, preparation, archiving, and quality control. In: Robertson G.P., Coleman D.C., Bledsoe C.S., Sollins P., (eds) Standard soil methods for long-termecological research. Oxford University Press, New York, pp 3–28.

Carrivick, J.L., Smith, M.W., Quincey, D.J., 2016. Structure from Motion in the Geosciences. John Wiley & Sons, Ltd, Chichester, UK.

Celi, L., Rosso, F., Freppaz, M., Agnelli, A., Zanini, E., 2010. Soil Organic Matter Characteristics in Sporadic Permafrost-affected Environment (Creux du Van, Switzerland). Arctic, Antarctic, and Alpine Research 42, 1–8. https://doi.org/10.1657/1938-4246-42.1.1

Cheng, H., Bai, R., Li, K., Zhao, C., Sun, S., Li, M., 2012. Study of loss or gain of soil organic carbon in Da’an region, Jilin Province in China. Journal of Geochemical Exploration 112, 272–275.

Colombo, N., Sambuelli L., Comina C., Colombero C., Giardino M., Gruber S., Viviano G., Vittori Antisari L. and Salerno F., 2018. Mechanisms linking active rock glaciers and impounded surface water formation in high-mountain areas. Earth Surface Processes and Landforms, 43(2), 417-431. DOI: 10.1002/esp.4257

D'Amico, M., Gorra, R., Freppaz, M., 2015. Small-scale variability of soil properties and soil–vegetation relationships in patterned ground on different lithologies (NW Italian Alps). CATENA 135, 47–58. https://doi.org/10.1016/j.catena.2015.07.005

Daniels, D.J., 2004. Ground Penetrating Radar. 2nd edition. Radar, Sonar, Navigation and Avionics Series 15, Institute of Electrical Engineers, London, UK.

Directive, H., 1992. Council Directive 92/43/EEC of 21 May 1992 on the conservation of natural habitats and of wild fauna and flora. Official Journal of the European Union 206, 7–50.

Dong, C., 1999. PowderX: Windows-95 based program for powderX-ray diffraction data processing. J Appl Crystallogr. 32:838.

Doolittle, J.A., Collins M.E., 1995. Use of soil information to determine application of ground penetrating radar. Journal of Applied Geophysics, 33: 101–108.

Léger, E., Dafflon B., Soom, F., Peterson J., Ulrich C., Hubbard, S., 2017. Quantification of Arctic Soil and Permafrost Properties Using Ground-Penetrating Radar and Electrical Resistivity Tomography Datasets, in IEEE Journal of Selected Topics in Applied Earth Observations and Remote Sensing, vol. 10, no. 10, pp. 4348-4359. doi: 10.1109/JSTARS.2017.2694447

Novàkovà, E., Karous, M., Zajiček, A., Karousovà, M., 2013. Evaluation of ground penetrating radar and vertical electrical sounding methods to determine soil horizons and bedrock at the locality Dehtáře. Soil & Water Res., 8 (3), pp. 105-112

FAO, 2014. World reference base for soil resources 2014: international soil classification system for naming soils and creating legends for soil maps. FAO, Rome.

Freppaz, M., Viglietti, D., Balestrini, R., Lonati, M., Colombo, N., 2019. Climatic and pedoclimatic factors driving C and N dynamics in soil and surface water in the alpine tundra (NW-Italian Alps). NC 34, 67–90. https://doi.org/10.3897/natureconservation.34.30737

Friedman, S.P., 2005. Soil properties influencing apparent electrical conductivity: a review. Comput. Electron. Agric. 46, 45–70.

Gerdol, R., Smiraglia, C., 1990. Correlation between vegetation pattern and microtopography in periglacial areas of the Central Alps. Pirineos 135, 13–28.

FAO, 2016. Guidelines for soil description, 4th ed. ed, 2006. . Food and Agriculture Organization of the United Nations, Rome.

Hagedorn, F., Mulder, J., Jandl, R., 2010. Mountain soils under a changing climate and land-use 5.

Hoffmann, U., Hoffmann, T., Johnson, E.A., Kuhn, N.J., 2014. Assessment of variability and uncertainty of soil organic carbon in a mountainous boreal forest (Canadian Rocky Mountains, Alberta). Catena 113, 107–121.

Islam A.K.M.E., Lotse, E.G. 1986. Quantitative mineralogical analysis of some Bangladesh soils with X-ray, ion exchange and selective dissolution techniques. Clay Miner. 21:31–42.

Otto, J.C., Sass, O., 2006. Comparing geophysical methods for talus slope investigations in the Turtmann valley (Swiss Alps), Geomorphology, Volume 76, Issues 3–4, 257-272. https://doi.org/10.1016/j.geomorph.2005.11.008.

Kneisel, C., Hauck, C., Fortier, R. and Moorman, B., 2008. Advances in geophysical methods for permafrost investigations. Permafrost Periglac. Process., 19: 157-178. doi:10.1002/ppp.616

Kneisel, C., 2006. Assessment of subsurface lithology in mountain environments using 2D resistivity imaging. *Geomorphology*, *80*(1-2), 32-44.

Knowles, J.F., Blanken, P.D., Lawrence, C.R., Williams, M.W., 2019. Evidence for non-steady-state carbon emissions from snow-scoured alpine tundra. Nat Commun 10, 1306. https://doi.org/10.1038/s41467-019-09149-2.

Leifeld, J., Zimmermann, M., Fuhrer, J., Conen, F., 2009. Storage and turnover of carbon in grassland soils along an elevation gradient in the Swiss Alps. Global Change Biology 15, 668–679. https://doi.org/10.1111/j.1365-2486.2008.01782.x

Loke, M.H., Barker, R.D., 1996. Rapid least-squares inversion of apparent resistivity pseudosections by a quasi-Newton method. Geophysical Prospecting, 44, 131-152 .

Magnani, A., Viglietti, D., Godone, D., Williams, M.W., Balestrini, R., Freppaz, M., 2017. Interannual Variability of Soil N and C Forms in Response to Snow—Cover duration and Pedoclimatic Conditions in Alpine Tundra, Northwest Italy. Arctic, Antarctic, and Alpine Research 49, 227–242. https://doi.org/10.1657/AAAR0016-037

McClymont, A. F., Hayashi, M., Bentley, L. R., Muir, D., Ernst, E., 2010. Groundwater flow and storage within an alpine meadow-talus complex, Hydrol. Earth Syst. Sci., 14, 859–872, https://doi.org/10.5194/hess-14-859-2010.

Mollaret, C., Hilbich, C., Pellet, C., Flores-Orozco, A., Delaloye, R., Hauck, C., 2019. Mountain permafrost degradation documented through a network of permanent electrical resistivity tomography sites. The Cryosphere 13, 2557–2578.

Prietzel, J., Christophel, D., 2014. Organic carbon stocks in forest soils of the German Alps. Geoderma 221–222, 28–39. https://doi.org/10.1016/j.geoderma.2014.01.021

Samouelian, A., Cousin, I., Tabbagh, A., Bruand, A., Richard, G., 2005. Electrical resistivity survey in soil science: A review, Soil Tillage Res., 83, 173 – 193, doi:10.1016/j.still.2004.10.004.

Schroter, D., 2005. Ecosystem Service Supply and Vulnerability to Global Change in Europe. Science 310, 1333–1337. https://doi.org/10.1126/science.1115233

Schuur, E.A.G., Abbott, B.W., Bowden, W.B., Brovkin, V., Camill, P., Canadell, J.G., Chanton, J.P., Chapin, F.S., Christensen, T.R., Ciais, P., Crosby, B.T., Czimczik, C.I., Grosse, G., Harden, J., Hayes, D.J., Hugelius, G., Jastrow, J.D., Jones, J.B., Kleinen, T., Koven, C.D., Krinner, G., Kuhry, P., Lawrence, D.M., McGuire, A.D., Natali, S.M., O'Donnell, J.A., Ping, C.L., Riley, W.J., Rinke, A., Romanovsky, V.E., Sannel, A.B.K., Schädel, C., Schaefer, K., Sky, J., Subin, Z.M., Tarnocai, C., Turetsky, M.R., Waldrop, M.P., Walter Anthony, K.M., Wickland, K.P., Wilson, C.J., Zimov, S.A., 2013. Expert assessment of vulnerability of permafrost carbon to climate change. Climatic Change 119, 359–374. https://doi.org/10.1007/s10584-013-0730-7

Smith, M.V., Carrivick J.L., Quincey D.J., 2015. Structure from motion photogrammetry. Physical Geography 40, 247–275.

Van Reeuwijk, L.P., 2002. Procedures for Soil Analysis. Technical Paper n. 9.

Wharton, R.P., Hazen, G.A., Rau, R.A., Best, D.L., 1980. Electromagnetic propagation logging--advances in technique and interpretation: Soc. Petr. Eng., 55th Annual Technical Conference, Paper 9267.

Zollinger, B., Alewell, C., Kneisel, C., Meusburger, K., Gärtner, H., Brandová, D., Ivy-Ochs, S., Schmidt, M.W.I., Egli, M., 2013. Effect of permafrost on the formation of soil organic carbon pools and their physical–chemical properties in the Eastern Swiss Alps. CATENA 110, 70–85. https://doi.org/10.1016/j.catena.2013.06.010

Figures

Figure 1: Location of the study area in the NW Italian Alps (www.pcn.minambiente.it), and overview of the study area (orthoimage Piemonte Region, year 2010) and photo (M. D'Amico). Solid and dashed lines indicate ERT and GPR profiles, respectively. Yellow lines indicate the profiles showed and discussed in the manuscript. Yellow circles identify the starting point of each geophysical profile. Cyan polygons indicate the location of the three soil profiles (P1, P2, and P3).

Figure 2. Soil profile P1 with sampling points scheme (numbers) and sectors (letters) in which C-stocks were estimated.

Figure 3. Soil profile P2 with sampling points scheme (numbers) and sectors (letters) in which C-stocks were estimated.

Figure 4. Soil profile P3 with sampling points scheme (numbers) and sectors (letters) in which C-stocks were estimated.

Figure 5. ERT sections: (a) ERT3 (long); (b) ERT2; (c) ERT5; (d) ERT6. The location of the ERT lines is reported in figure 1. Short sections are cut at 1.5-m depth.

Figure 6. GPR results. (a) Zoom on GPR4 section with tentative interpretation of the shallow stratigraphy: soil (s), soil-to-bedrock transition (t), bedrock (b). (b, d, f) Processed radargrams for lines GPR4, GPR8, GPR5 (vertical cut at 1.5-m depth). (c, e, g) Soil bottom estimation on the above sections. Comparison between the location of the electrical resistivity gradient maxima computed on the ERT lines of Figure 5 (red dots) and the piking of the different layers on GPR results as shown in Figure 6a (in blue, dotted line: s-t interface, dashed line t-b interface). The location of the GPR profiles is reported in Figure 1.

Tables

Sample number	Horizon	Munsel colour, moist	Stone fragments (%)	Clay (%)	Silt (%)	Sand (%)	Textural class	Structure	pH	TOC ($g*kg^{-1}$)	TN ($g*kg^{-1}$)	TOC/TN	BD ($kg*m^{-3}$)	TH (m)	VF	C-STOCK ($kg*m^{-2}$)
P1																
1	A2	10YR 3/2	30	2.81	14.54	82.65	LS	SB	4.8	19.02	0.97	20	1000	0.20	0.70	2.66
2	A1	10YR 3/2	30	2.54	14.95	82.51	LS	SB	4.4	10.77	0.80	13	1000	0.30	0.70	2.26
3	BA	10YR 3/3	40	1.59	23.25	75.16	LS	BL	4.8	4.74	0.44	11	1200	0.20	0.60	0.68
4	A1+A2	10YR 3/2	40	2.69	15.35	81.96	LS	GR	4.7	12.04	1.05	11	1000	0.30	0.60	2.17
5	A	10YR 3/2	80	2.69	14.45	82.86	LS	GR	4.4	18.58	1.47	13	1000	0.20	0.20	0.74
P2																
6	A	10YR 2/1	30	2.64	20.85	76.51	LS	SB	4.3	8.00	0.76	11	1000	0.20	0.70	1.12
7	A@	10YR 3/2	10	2.29	23.25	74.46	LS	PL/SB	5.6	20.53	1.08	19	1100	0.05	0.90	1.02
8	A2	10YR 3/3	30	1.89	18.30	79.81	LS	SB	4.7	10.95	0.79	14	1000	0.20	0.70	1.53
9	A1	10YR 3/2	70	2.54	12.09	85.37	LS	GR	4.4	11.30	1.05	11	1000	0.10	0.30	0.34
10	BC	10YR 4/4	70	1.43	27.56	71.01	SL	PL/SB	5.3	1.40	BDL	-	1200	0.20	0.30	0.10
11	CB	10YR 5/2	70	1.04	26.31	72.65	LS	SB	5.9	BDL	BDL	-	1200	0.20	0.30	0.00
12	BW	10YR 3/4	60	0.89	25.75	73.36	LS	SB	5.2	2.56	0.29	9	1200	0.20	0.40	0.25
13	A	10YR 3/2	30	4.33	24.12	71.55	SL	BL	4.8	10.94	0.77	14	1000	0.15	0.70	1.15
14	BA	10YR 3/3	50	2.84	29.25	67.91	SL	CO/PR	4.9	11.00	0.72	15	1200	0.20	0.50	1.32
15	A	10YR 3/2	10	3.89	14.00	82.11	LS	GR	4.5	7.13	0.91	8	1000	0.15	0.90	0.96
16	Silt caps	10YR 6/4	10	6.24	41.90	51.86	SL	PL	5.0	2.76	0.33	8	1300	0.03	0.90	0.10
P3																
1	A1	10YR 2/1	70	4.29	8.05	87.66	S	GR	4.9	5.62	0.45	12	1000	0.05	0.30	0.08
2	A2	10YR 3/2	5	3.24	15.60	81.16	LS	GR	4.9	8.72	0.50	17	1000	0.28	0.95	2.28
3	A2	10YR 3/2	5	4.23	15.64	80.13	LS	CO	4.9	10.47	0.70	15	1000	0.25	0.95	2.49
4	A2	10YR 3/2	20	4.84	28.24	66.93	SL	CO	4.8	7.56	0.52	14	1000	0.25	0.80	1.51
5	A2	10YR 3/2	0	4.82	20.75	74.44	SL	SG	4.7	11.82	0.69	17	1000	0.05	1.00	0.59
6	Bw	10YR 5/4	20	2.64	31.85	65.51	SL	SB	5.0	1.46	0.22	7	1200	0.25	0.80	0.35

7	BC	10YR 4/3	50	3.39	16.75	79.86	LS	SB	5.2	2.42	0.24	10	1200	0.20	0.50	0.29
8	A2	10YR 3/2	0	2.77	13.73	83.50	LS	GR	4.9	8.09	0.47	17	1000	0.02	1.00	0.16
9	BC	10YR 4/3	70	4.64	19.50	75.86	LS	PL	5.1	3.07	0.33	9	1200	0.20	0.30	0.22
10	Bw	10YR 3/4	40	3.34	19.55	77.11	LS	SB	5.2	1.65	0.21	8	1200	0.30	0.60	0.36

Table 1. Morphological, physical and chemical properties of the soil profiles. Textural class: LS=loamy sand; SL=sandy loam. Structure: SB=subangular blocky; BL=blocky; GR=granular; PL=platy; CO=columnar; PR=prismatic; SG=single grain. BDL=below detection limit.

P1			
Sector	**Horizon**	**Sample number**	**C-STOCK$_{tot}$ (kg*m^{-2})**
A	A1 A2 BA	2 1 3b	5.18
B	A1+A2 BA	4 3	2.85
C	A	5	0.74
P2			
D	A	6	1.12
E	A1 A2 A@	9 8 7	2.89
F	A1 A2 A@ BC CB	9 8 7 10 11	2.99
G	A Bw BC	13 12 10b	1.50
H	A BA Silt caps	15 14 16	2.38
P3			
I	A1 A2 A2 Bw	1 2 5 6	3.30
J	A1 A2 A2 BC	1 3 8 7	3.02
K	A1 A2 Bw BC	1 4 10 9	2.17

Table 2. Total C-stock of the profiles for each sector.

Figure1

Click here to download high resolution image

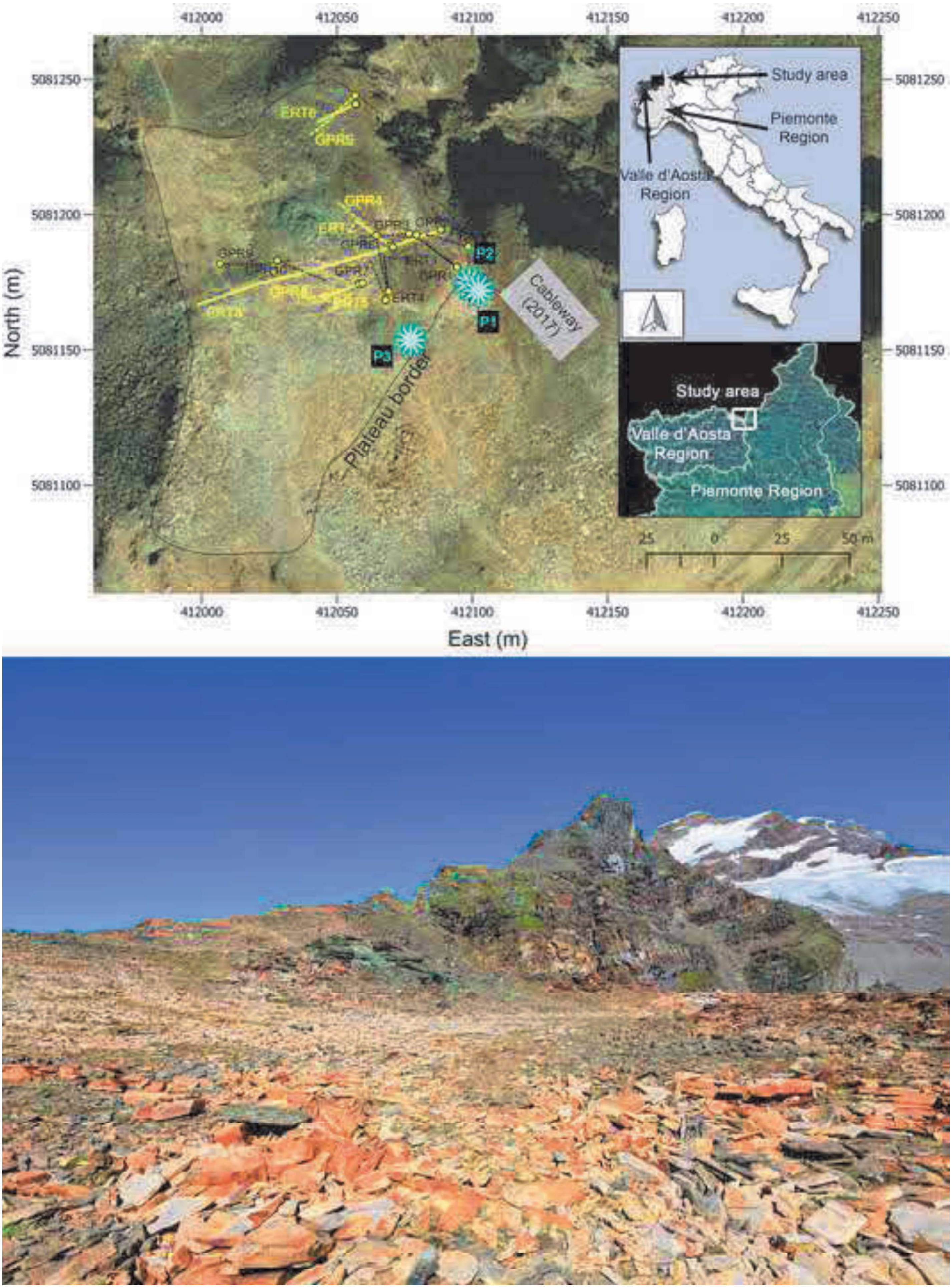

Figure2
Click here to download high resolution image

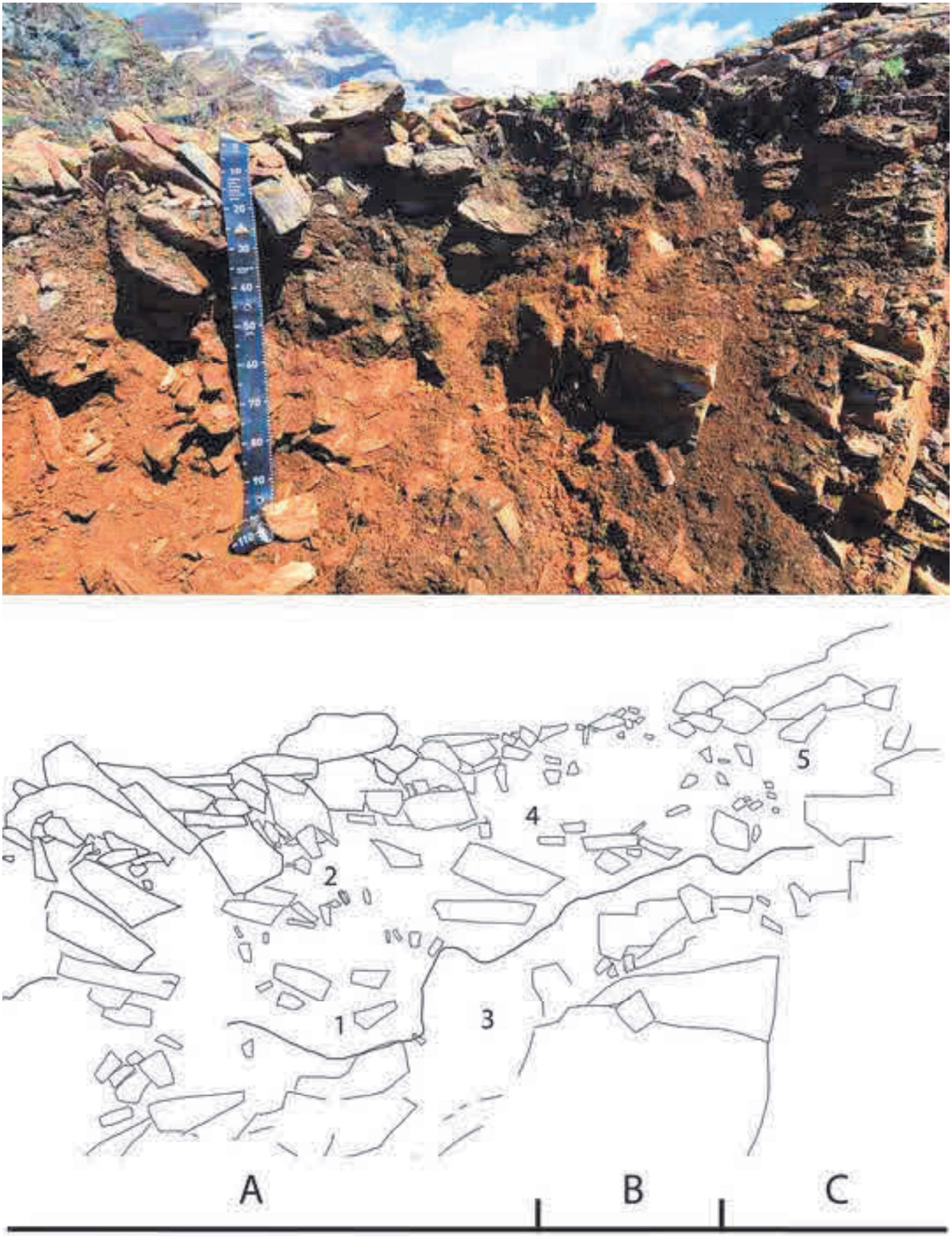

Figure3

Click here to download high resolution image

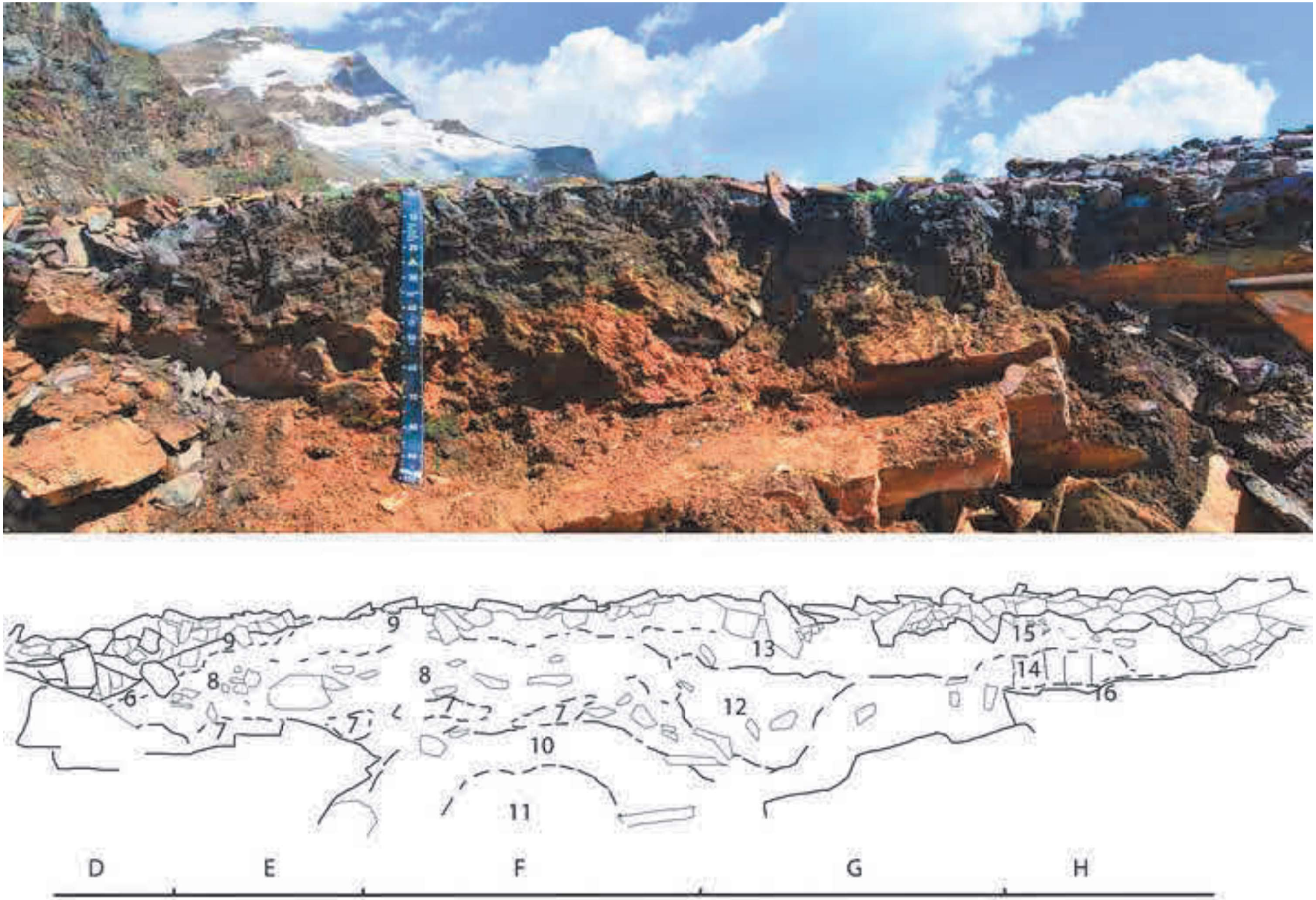

Figure4
Click here to download high resolution image

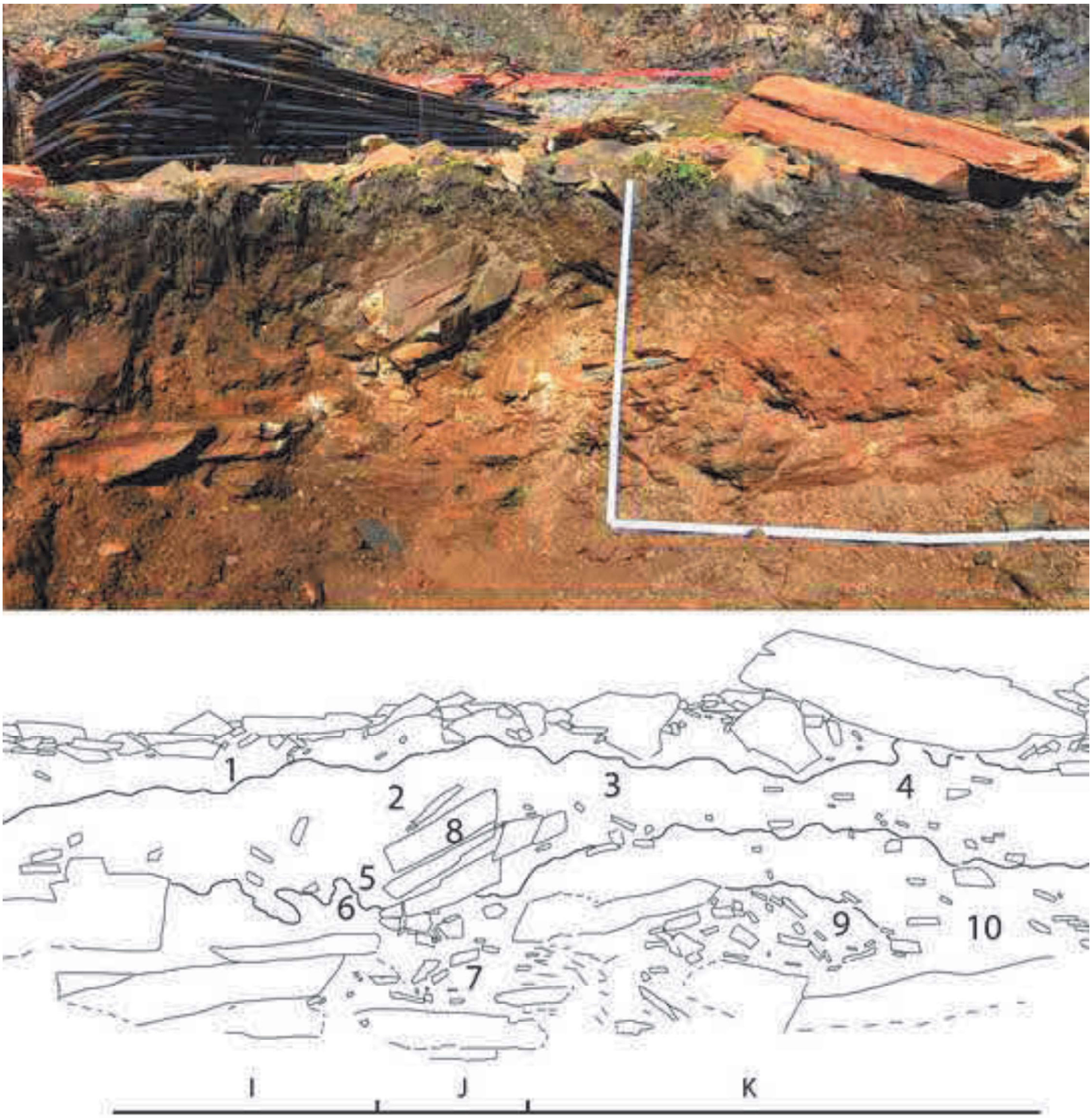

Figure5

Click here to download high resolution image

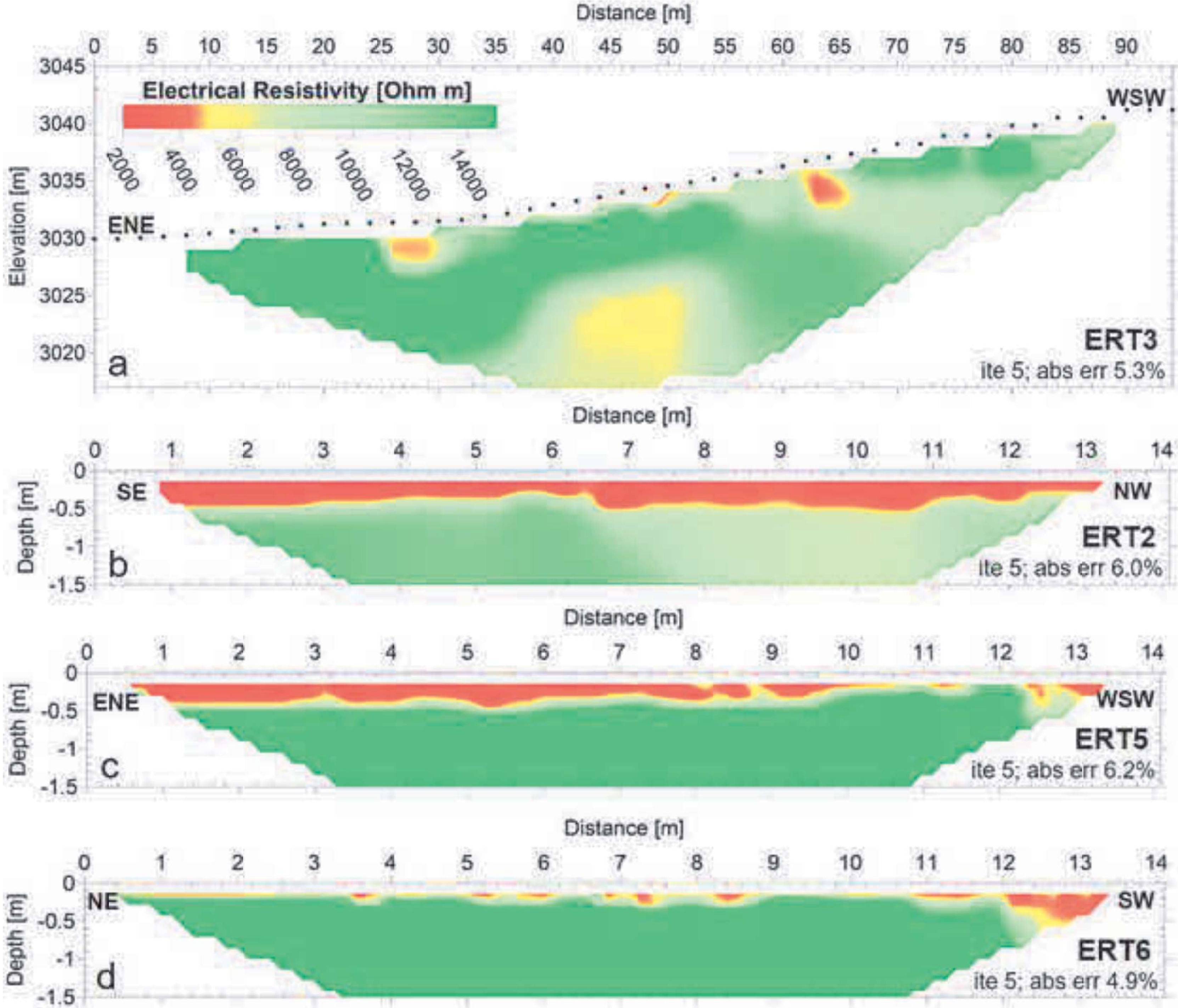

Figure6

Click here to download high resolution image